Modelling dynamic pantograph loads with combined numerical analysis

F. F. Jackson[1] · R. Mishra[1] · J. M. Rebelo[2] · J. Santos[2] · P. Antunes[2,3] · J. Pombo[2,3,4] · H. Magalhães[3] · L. Wills[5] · M. Askill[6]

Abstract

Appropriate interaction between pantograph and catenary is imperative for smooth operation of electric trains. Changing heights of overhead lines to accommodate level crossings, overbridges, and tunnels pose significant challenges in maintaining consistent current collection performance as the pantograph aerodynamic profile, and thus aerodynamic load changes significantly with operational height. This research aims to analyse the global flow characteristics and aerodynamic forces acting on individual components of an HSX pantograph operating in different configurations and orientations, such that the results can be combined with multibody simulations to obtain accurate dynamic insight into contact forces. Specifically, computational fluid dynamics simulations are used to investigate the pantograph component loads in a representative setting, such as that of the recessed cavity on a Class 800 train. From an aerodynamic perspective, this study indicates that the total drag force acting on non-fixed components of the pantograph is larger for the knuckle-leading orientation rather than the knuckle-trailing, although the difference between the two is found to reduce with increasing pantograph extension. Combining the aerodynamic loads acting on individual components with multibody tools allows for realistic dynamic insight into the pantograph behaviour. The results obtained show how considering aerodynamic forces enhance the realism of the models, leading to behaviour of the pantograph–catenary contact forces closely matching that seen in experimental tests.

Keywords Pantograph–catenary interaction · Pantograph aerodynamics · Computational fluid dynamics · Pantograph loads · Current collection performance

1 Introduction

In electric rail transport, the interaction between the pantograph and overhead line is critical. Insufficient upward force can result in poor contact and hinder current collection, resulting frequently in electrical arcing, which can damage the components. Excessive uplift force can lead to high wear on the collector strips and contact wire. Typically, the pantographs are assembled with a pneumatic system that controls the upward force that the pantograph head applies on the overhead line. The pneumatic pressure is regulated to maintain the force within prescribed standards (e.g. EN50367:2012 [1]).

Since the pantograph is located on top of the train, it is exposed to harsh environmental conditions. As the train speed increases, the aerodynamic loads become more significant, effecting the contact force between the collector strips and the contact wire [2]. The total contribution of the interaction force is thus a contribution of the pneumatic force and the aerodynamic load. Severe aerodynamic loads, including crosswinds or trains travelling through tunnels, can lead to dewirement and significant damage to the overhead equipment. Adding complexity to the aerodynamic issues is the asymmetry in modern pantograph designs and its relative position on the top of the train. The asymmetry

✉ F. F. Jackson
F.F.Jackson@hud.ac.uk

1 School of Computing and Engineering, University of Huddersfield, Huddersfield, UK

2 School of Computing and Engineering, Institute of Railway Research, University of Huddersfield, Huddersfield, UK

3 IDMEC, Instituto Superior Técnico, Universidade de Lisboa, Lisbon, Portugal

4 ISEL, Instituto Politécnico de Lisboa, Lisbon, Portugal

5 Hitachi Rail, Newton Aycliffe, UK

6 Wabtec/Brecknell Willis, Chard, UK

means that its orientation (knuckle-leading and knuckle-trailing) plays a significant role on the total aerodynamic loading. Furthermore, the geometry and layout of components on the roof of the train can cause significant turbulent effects upstream of the pantograph, causing dynamic oscillations in the frequency range of the assembly. All this has led to considerable research interest into the modelling of pantograph systems [3].

One specific area which has recently received considerable attention is the use of computational fluid dynamics (CFD) in the investigation of pantograph aerodynamics. Luo et al. [4] employed a Reynolds averaged Navier–Stokes (RANS) analysis to examine simplified pantograph models on a full train. Their goal was to identify the optimal placement of the pantograph, taking into account the forces experienced and crosswinds. Dai et al. [5] used RANS modelling to investigate the use of pantograph baffles (also referred to as wings or vanes) to minimize the variation in the total uplift force generated for each orientation of the pantograph. Using the same approach, Dai et al. [6] also investigated the aerodynamic influence of the collectors spacing on double-strip pantographs. They found that regardless of orientation, the increased strip spacing resulted in increased drag and lift forces. Xiao et al. [7] used transient improved delayed detached eddy simulation (IDDES) to investigate the effect of the platform depth on the aerodynamic performance. Their results revealed that a pantograph experiences a significant shielding effect when operating on a sunken platform. Li et al. [8] used transient detached eddy simulations (DES) to investigate the forces acting on a pantograph at different operational heights both in the knuckle-leading and knuckle-trailing configuration. Their research showed an increased drag force for the pantograph in the knuckle-trailing (downstream) configuration and an approximate linear relationship between the drag force and operational hight for both orientations. Li et al. [9] used the delayed-DES (DDES) to investigate the effects of yaw angle on aerodynamic performance and flow field characteristics.

In addition to the aforementioned classical CFD based investigations, there have been a number of studies utilizing the Lattice Boltzmann method (LBM) [10–12] as a means to obtain general flow field information. There has also been interest in the use of CFD to include the simulation of aerodynamic induced noise. Kim et al. [13] investigated the influence of different roof geometries of the sunken platform holding the pantograph for the analysis of aerodynamic noise. The aeroacoustics properties of isolated pantographs have also been modelled by Zhang et al. [14] and AbdelGawad et al. [15].

Further to trains running in an open environment, attention has been directed towards the aerodynamic behaviour of trains passing through tunnels, as this increases the relative air velocity experienced by the train. Ji et al. [16] coupled CFD with multibody dynamics to investigate aerodynamic effects on the pantograph of a train passing through a tunnel. Niu et al. [17] looked at trains passing through tunnels to examine the global pressure distribution. Li et al. [18] investigated the aerodynamic effect on the pantograph of a train passing through a tunnel and compared finite element models with free air conditions. It was found that, for the train running through the tunnel, the aerodynamic lift and drag forces increased on the pantograph.

To gain an in-depth understanding of the pantograph behaviour with aerodynamic loads, the force on different pantograph components has been explored by Carnevale et al. [19, 20] both in the knuckle-leading and knuckle-trailing configuration. Here, the authors show how steady state, RANS methods can be used to effectively capture static aerodynamic forces through validation with wind tunnel experiments. With the computed results, the principle of virtual work was used to determine the total upward force exerted by the pantograph. In this work the roof structure of the train was approximated through the inclusion of an obstacle upstream of the pantograph, providing aerodynamic shielding. However, the full train geometry was not considered.

As highlighted above, there has been considerable research into the modelling of pantograph systems in terms of aerodynamic performance. However, there is still a need for a full investigation into the total aerodynamic loading of pantograph components at different operational heights and orientations, and how this affects the interaction with the overhead contact line. Additionally, investigations should incorporate the full train geometry to provide a more representative and accurate analysis of the pantograph aerodynamics.

In this study, an analysis of the aerodynamic loads experienced by the main pantograph components under various operating heights (i.e. low, normal, and high) and configurations (i.e. knuckle-leading and knuckle-trailing) is presented. Figure 1 illustrates the Wabtec/Brecknell Willis HSX pantograph used in this research and highlights the components considered in the analysis. The pantograph is placed on a sunken platform on the roof of a Hitachi Class 800 train, allowing for the accurate representation of the entire flow field and, thus, reliable determination of aerodynamic forces. The computed component forces are then incorporated into dynamic multi-body simulations to allow for dynamic prediction of the pantograph loads under variation in operational height.

The remainder of the paper is organized as follows: Sect. 2 describes the details of the computational modelling and mesh sensitivity analysis. Section 3 provides aerodynamic results for each of the different operational heights and orientations and forces acting on each pantograph component. Section 4 presents application examples to demonstrate the methodology proposed here. It combines
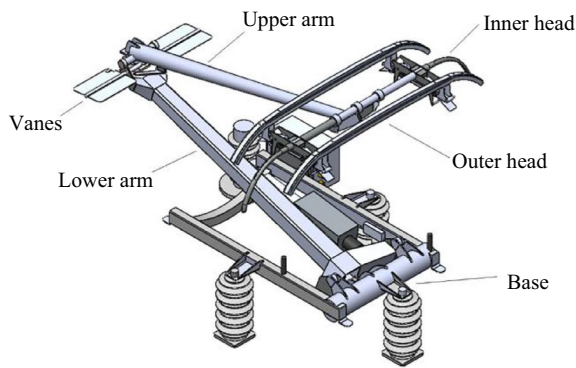
Fig. 1 Illustration of HSX pantograph assembly and named components

the aerodynamic results with a multibody formulation in order to understand how the current collection performance is affected by the pantograph air flow conditions. Finally, concluding remarks are given in Sect. 5.

2 Methodology

2.1 Computational model

The commercially available computational fluid dynamics software, ANSYS Fluent, is used in this work. This software operates based on the Navier-Stokes equations, which are subsequently discretized using the finite-volume method. A steady state, RANS solutions is obtained, where the shear stress transport (SST) k-ω turbulence model is used for closing the governing equations. This two-equation model has proven effective in handling adverse pressure gradients [21] and has been utilized for comparable pantograph investigations [19, 20]. The remaining numerical set-up is as follows: for pressure–velocity coupling, the 'coupled' scheme is utilized with Rhie-Chow: distance-based flux type, and second-order upwind schemes are adopted for momentum, turbulence kinetic energy, and specific dissipation rate. Gradients are calculated with the least squares cell-based method.

To ensure that the pantograph is modelled in a representative setting, a simplified model of a Class 800 train is configured, with the pantograph placed on a sunken platform on the roof, providing the aerodynamic shielding to the components of the lower pantograph assembly. Emphasis is placed primarily on capturing the shape of the upper surface of the train, such as the roof and cavity as these surfaces are assumed to have the most significant impact on the flow. Consequently, as in Refs. [5, 6, 13, 16, 19] complex assemblies on the lower surface of the train, such as track, wheels and bogies are neglected to reduce

modelling complexity. The pantograph platform depth is set to 570 mm recessed from the top of the train based on available technical documentation. The full model is illustrated in Fig. 2 for both knuckle-leading and knuckle-trailing configurations. This figure further highlights the distance from the front of the train with respect to the direction of travel.

The computation domain is illustrated in Fig. 3. Here, the domain is scaled according to the height of the train, H, which is 3520 mm. The ground is simulated as a no-slip wall with a nonzero velocity component, set to the inlet velocity value of 200 km/h. The top, left, and right sides of the domain are treated as symmetry. The outlet surface has the atmospheric pressure assigned, and all the remaining solid surfaces are treated as standard no-slip, zero velocity.

2.2 Mesh sensitivity analysis

The spatial discretization (mesh generation) of the pantograph-train system is performed with the Fluent mesh generator. A combination of both polyhedral and hexahedral elements is used, with a refinement zone surrounding the pantograph and wake region. Inflation layers are added to the solid zero-velocity no-slip surfaces of the train and
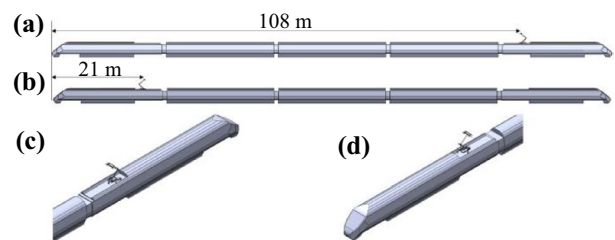
Fig. 2 Illustration of pantograph location in **a** knuckle-trailing and **b** knuckle-leading. Images **c** and **d** further illustrate the recessed cavity for knuckle-trailing and knuckle-leading orientations, respectively
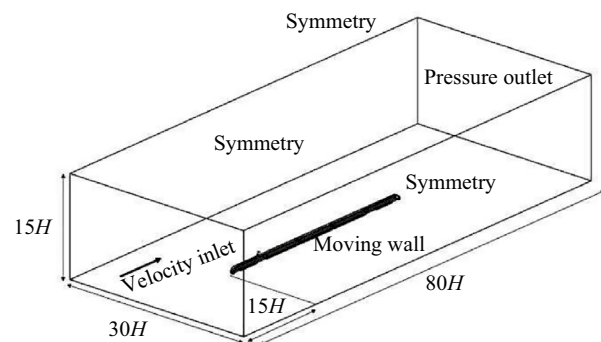
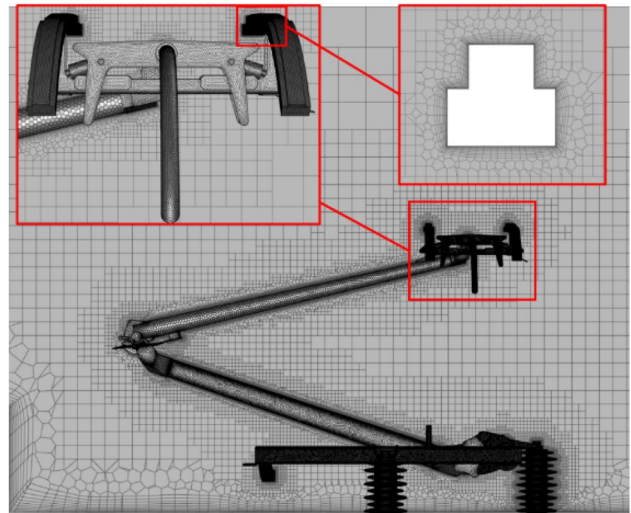**Fig. 3** Computational flow domain and assignment of boundary conditions

pantograph assembly. The knuckle-leading pantograph, in the normal operating configuration is chosen as the base case for the mesh analysis. Each of the simulations perform 250 iterations, as this is determined to be sufficient for stable force values to be observed for each of the components. A total of six different mesh cases are tested, with increasing cell count. The local size control parameters are displayed in Table 1. The coarsest of these meshes comprised of approximately 6.4 million cells, whereas the finest totalled over 33.9 million.

For each of the simulations, the lift and drag force acting on each of the identified components, illustrated in Fig. 4b are monitored as a means of determining the convergence level. An example of the recorded drag force is displayed in Fig. 4a. As it can be seen, the force values vary significantly in the first few iterations. However, after approximately 100 iterations, the values become stable, with only relatively small oscillations. The force values are therefore averaged over the remaining 150 iterations to remove the influence of the small oscillations.

The error between successive mesh refinements is compared for each of the components. For the chosen mesh setting (mesh 5 in Table 1) the average force error is less than 5% than the finest mesh tested. Thus, mesh 5 is deemed as suitable in terms of accuracy and computational requirements. An illustration of the final mesh is displayed in Fig. 5. Here, magnified zones are highlighted to illustrate the mesh refinement and inflation layers added to the no-slip wall surfaces.

Table 1 Mesh independence control parameters

| Mesh number	Minimum element size (m)	Control volume size (m)	Face control size (m)	Cells
1	0.0020	None	0.010	6,439,996
2	0.0020	None	0.008	8,210,565
3	0.0020	0.080	0.006	8,700,000
4	0.0020	0.060	0.004	13,460,948
5	0.0020	0.055	0.003	15,290,843
6	0.0015	0.050	0.002	33,937,447

Fig. 5 Generated poly-hexacore mesh around the pantograph assembly, with boxes highlighting local face sizing control and inflation layers
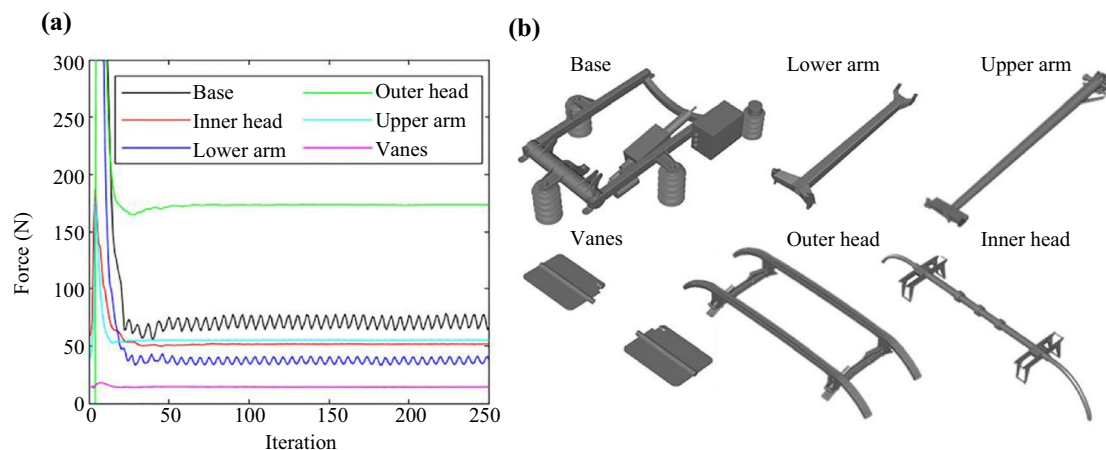
Fig. 4 Illustration of **a** component drag force measurement values, and **b** individual pantograph components monitored in the analysis

2.3 Methodology validation

To verify the computational results, benchmark tests are performed using a wind tunnel and a 1/50th scale model of the front section of the train. In these tests, the total drag force acting on the train is measured and compared to the predicted values from an equivalent CFD model. Mesh controls are applied such that variation in y^+ values can be examined to determine the effect on the results, with values ranging from $y^+ < 10$ to $y^+ > 200$. The air velocity U is varied from 13 m/s up to the maximum value, U_{max}, of 37 m/s while the resulting drag force is recorded. For each of the tests, the computed Reynold's number is above 10,000, thus the flow is considered to be fully turbulent. As shown in Fig. 6, there is good agreement between the experimental and CFD values. Although for each of the tests the CFD results slightly overestimated the experimental drag force, the results above 32 m/s produce an error of less than 5% and thus are deemed suitable for the subsequent analysis. Furthermore, CFD results with $y^+ > 200$ also remained within the acceptable error of less than 5%.
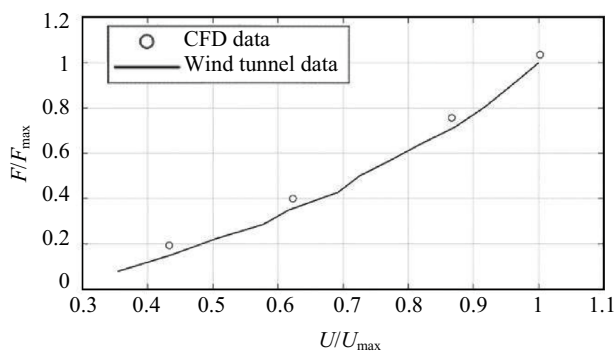
Fig. 6 Normalized drag force results of CFD and wind tunnel validation

3 Pantograph aerodynamic studies

The pantograph aerodynamic studies are divided into three sections. First, the pantograph configurations considered here are described, representing three different levels of extension. Then, the flow field around the train and pantograph are analysed both qualitatively and quantitatively. Finally, the resulting forces on the pantograph and its individual components are investigated for each configuration and orientation.

3.1 Pantograph configurations

Three pantograph heights are considered, which are illustrated in Fig. 7. These consist of a low, normal, and high extension, corresponding to 320, 860, and 2100 mm, respectively. The overall height of the pantograph head is determined by the angle of the lower and upper arms. As these change, also the connected vanes change their angle of attack. The angle of the vanes for each height is determined from measurements taken of the connecting rod on the physical pantograph and the corresponding upper arm angle in the provided CAD geometry. A summary of each of the angles for each of these components is given in Table 2.

Irrespective of the pantograph height, the head of the pantograph is always assumed to be parallel to the ground. Unlike the lower arm, upper arm and vanes, the force

Table 2 Component angles (degrees) for each configuration

Configuration	Lower arm	Vanes	Upper arm
Low	8.1	2.9	2.8
Normal	18.1	4.7	13.0
High	43.0	12.3	38.4
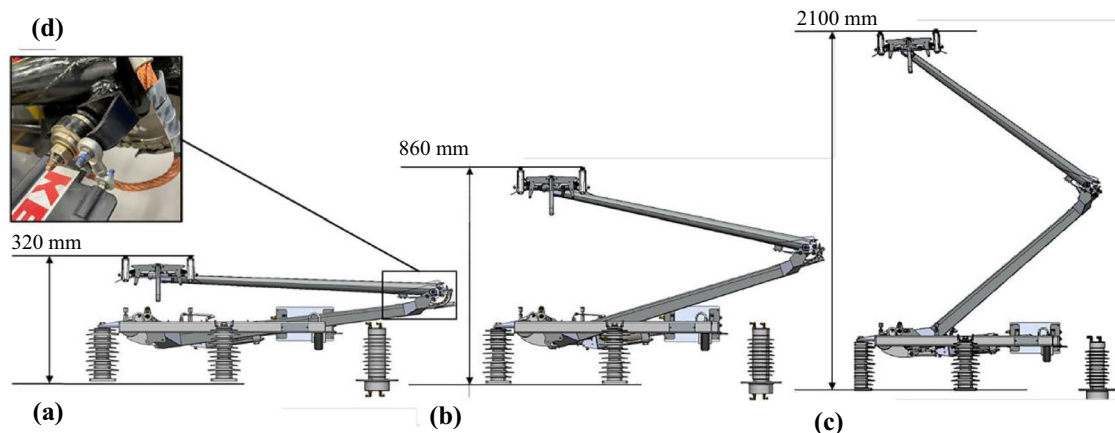
Fig. 7 Pantograph operational heights: **a** low, **b** normal, and **c** high. Image **d** illustrates the connection between the vanes and upper arm

variation in the pantograph head will be completely determined by the relative upstream flow conditions rather than change in orientation.

3.2 Flow field analysis

The upstream geometry of the knuckle-leading pantograph is considerably different from that of the knuckle-trailing. For the former, the pantograph is positioned close to the front carriage, whereas the latter is positioned towards the rear of the train. The boundary layer for these two pantographs is, therefore, significantly different. The mid-plane velocity magnitude contours are displayed in Fig. 8 for each pantograph height and orientation. In Fig. 8a, b, and c, the knuckle-leading configuration is displayed, for the low, normal, and high configuration, respectively. For the pantograph in the low configuration, it is clear that a significant proportion of the lower assembly is within a low velocity magnitude zone of

recirculating flow due to the presence of the sunken platform. As the pantograph height increases to the normal configuration, the lower arm extends beyond the depth of the sunken platform, experiencing a relatively larger upstream velocity. It is also further apparent that in the normal configuration, a significant wake region is formed behind the pantograph. Finally, in the highest configuration, the wake which formed behind the pantograph becomes segmented, with noticeable disturbance around the head and lower assembly and relatively less around the upper arm section. Similar observations are observed in the knuckle-trailing orientation, depicted in Fig. 8d, e, and f, although it appears that the wake regions, in the high configuration, begin to merge due to flow disturbance around the sunken platform step, channeling flow upwards.

To quantify the flow characteristics experienced by the pantograph, plots of the velocity profile are extracted at different locations upstream and downstream of the pantograph. The plot locations of these upstream and downstream
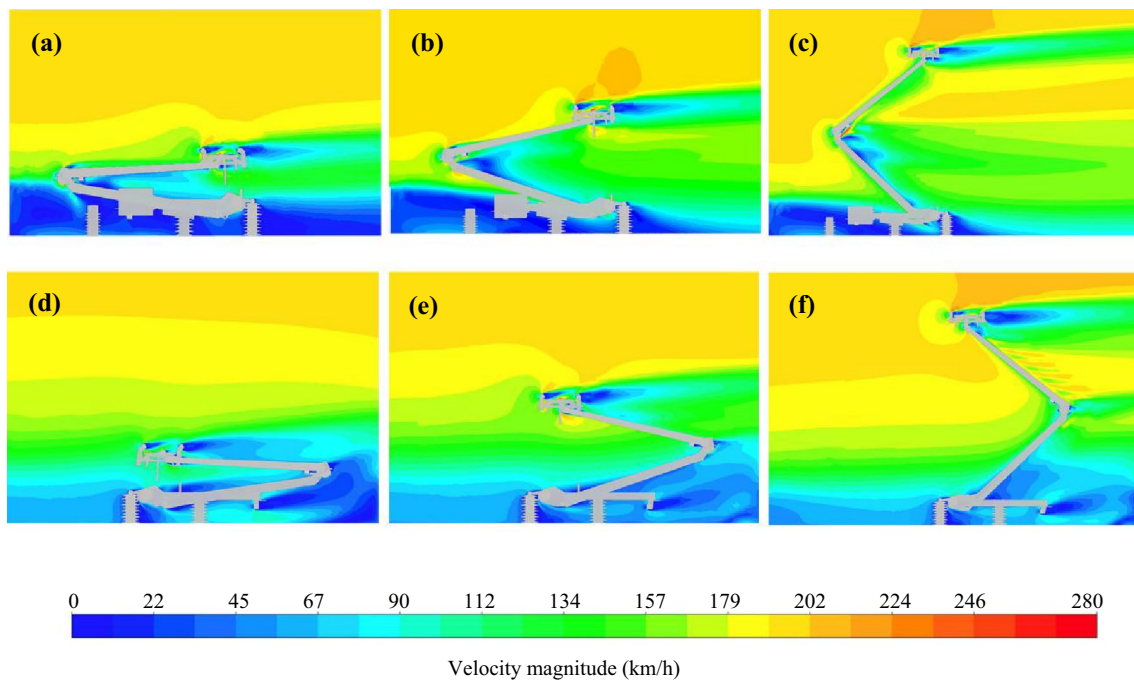
Fig. 8 Mid-plane velocity magnitude contours for knuckle-leading: **a** low, **b** normal, and **c** high configuration, and for knuckle-trailing: **d** low, **e** normal, and **f** high configuration
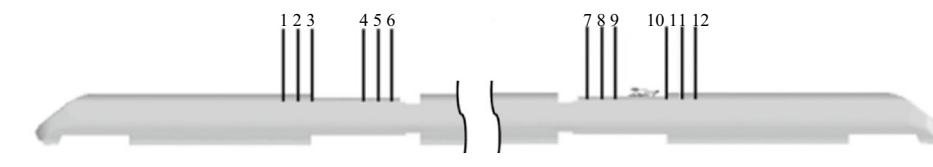
Fig. 9 Illustration of upstream and downstream lines used for obtaining velocity magnitude data

lines, for both the knuckle-leading and knuckle-trailing pantograph, are displayed in Fig. 9. These lines are grouped with 1 m separation, with a 2.5 m spacing around the pantograph.

The resulting velocity magnitude plots for the knuckle-leading pantograph are displayed in Fig. 10, where L is the streamwise displacement taken from the furthest velocity measurement location upstream of the pantograph. In each of these figures, black lines display the upstream and red lines the downstream velocity magnitude profile. It is worth mentioning that, in order to compare normalized results, each of the lines are of the same length, and all start at the same height, i.e. that of the sunken platform. This results in a visual abrupt step in the plots for the lines which intersect the train body (black lines in Fig. 10 and red lines in Fig. 11). For the knuckle-leading orientation, displayed in Fig. 10a, b and c for the low, normal, and high configurations, respectively, the upstream velocity is fully developed, with little variation between each of the measurement

locations. With the pantograph in the low configuration, the disturbance downstream is locally concentrated. As the pantograph height increases, the disturbance becomes more pronounced, with a clear reduction in velocity behind the head region, represented by the spikes at $H/H_0 \approx 0.5$.

For the knuckle-trailing orientation, depicted in Fig. 11a, b and c for the low, normal, and high configurations, respectively, the upstream flow can be observed to not be fully developed, changing as it approaches the pantograph. Furthermore, the profile is notably different than that of the knuckle-leading configuration, highlighting the importance of consideration of the full train geometry in the aerodynamic analysis. For the low configuration, represented in Fig. 11a, change in velocity magnitude profile is minimal. As the height increases to the normal and high configuration, the downstream flow disturbance becomes more pronounced.

When comparing the two pantograph orientations, it becomes evident that the downstream velocity profiles are
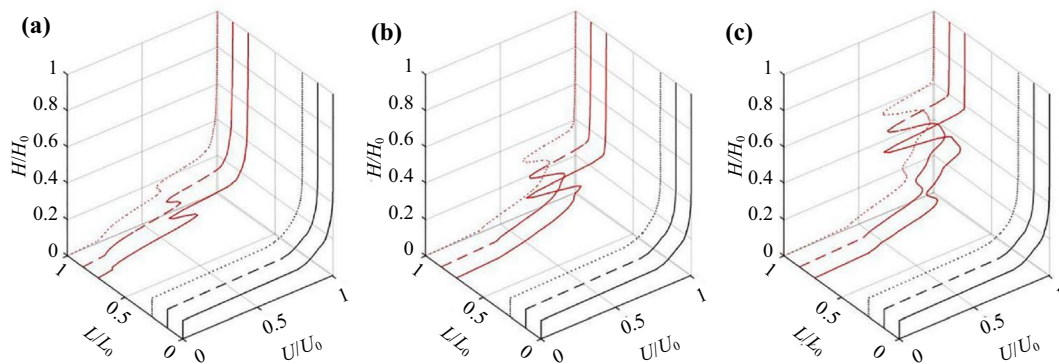
Fig. 10 Velocity magnitude profiles for knuckle-leading pantograph in **a** low, **b** normal, and **c** high configuration ($H_0 = 5$ m, $L_0 = 7.5$ m, $U_0 = 55.56$ m/s). Black lines are upstream of the pantograph and red lines downstream
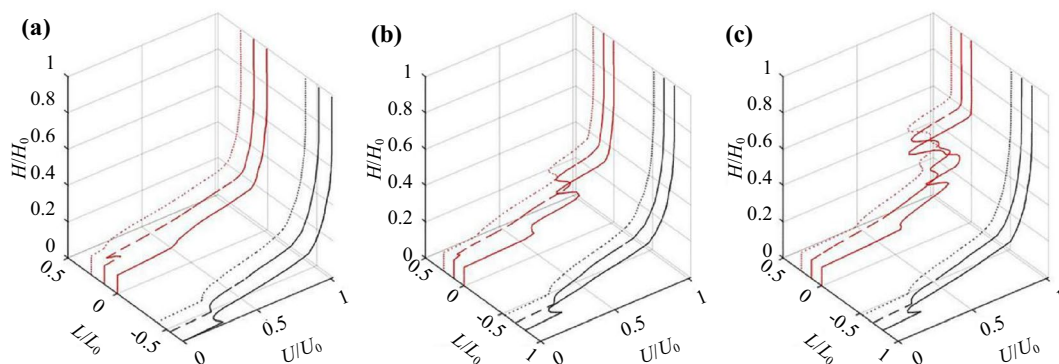
Fig. 11 Velocity magnitude profiles for knuckle-trailing pantograph in **a** low, **b** normal, and **c** high configuration. Black lines are upstream of the pantograph and red lines downstream

much more disturbed when in the knuckle-leading orientation for each of the operational heights. However, both orientations exhibit a noticeable increase in disturbances as the pantograph height increases.

In addition to the velocity data, the mid-plane pressure contours are displayed in Fig. 12a, b, and c for the knuckle-leading orientation in the low, normal, and high configuration, respectively. Here it is clear to see the significant pressure difference between the low and high configurations. The positive and negative static pressure contours around the head noticeably increase in size with increasing operational height. Furthermore, in the high configuration, there is a considerable concentration of negative pressure behind the knee joint of the lower and upper arms, indicative of large drag forces. For the knuckle-trailing orientation, depicted in Fig. 12d, e, and f for the low, normal, and high configurations, respectively, the same trend of positive and negative pressure distribution around the head section can be observed. However, in the high configuration, the pantograph displays significant concentration of high-pressure in front of the knuckle region.

3.3 Pantograph component aerodynamic forces

The upward contact forces exerted by the pantograph on the overhead line is the key consideration for effective current collection. The assembly of the pantograph means that both the lift and drag forces acting on different components have a significant impact on the overall upward force. The total aerodynamic force acting on a body is a combination of the pressure and viscous force. These values are easily extracted from CFD software, whereas obtaining these values experimentally poses significant challenges, especially on an individual component basis. In Table 3, the combined

-1500 -1260 -1020 -780 -540 -300 -60 180 420 660 900 1140 1500

Velocity magnitude (km/h)
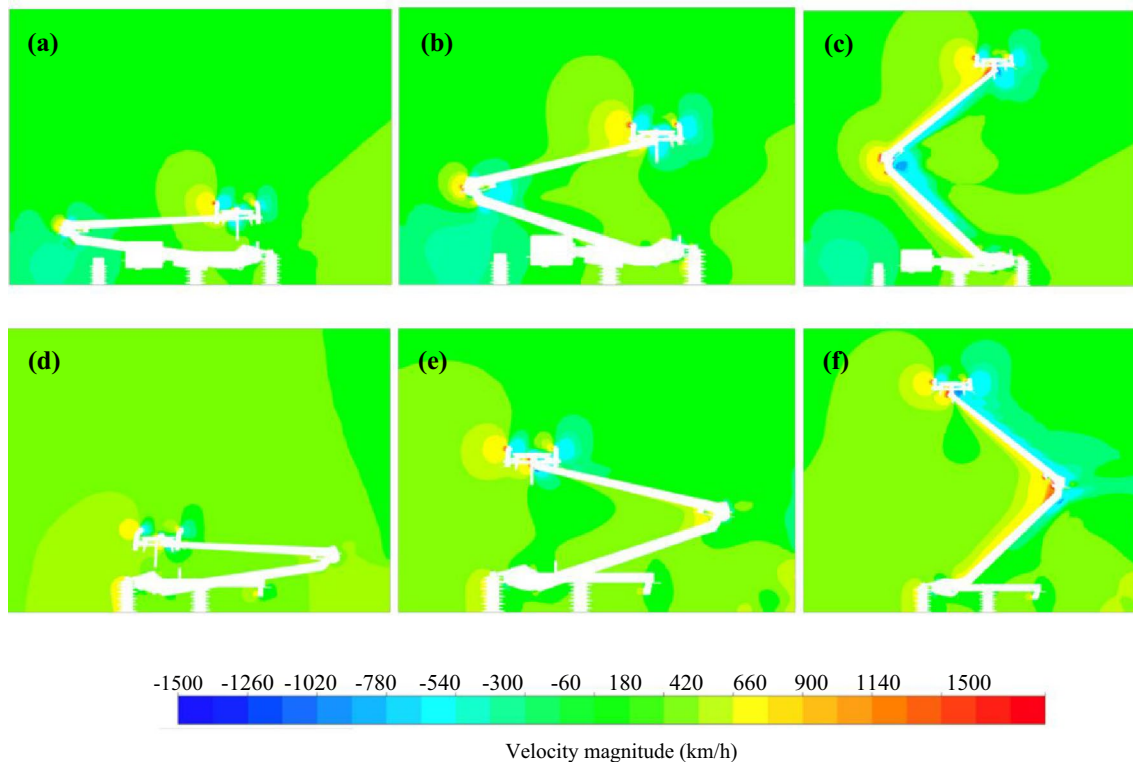
Fig. 12 Mid-plane static pressure contours for knuckle-leading: **a** low, **b** normal, and **c** high configuration, and for knuckle-trailing: **d** low, **e** normal, and **f** high configuration

Table 3 Drag force values for knuckle-leading pantograph (unit: N)

Configuration	Base	Lower arm	Vanes	Upper arm	Inner head	Outer head
Low	59.2	19.6	8.4	31.6	41.3	142.9
Normal	70.8	37.4	14.4	55.2	51.6	173.5
High	55.9	107.8	37.3	118.1	60.9	183.4

viscous and pressure drag force values are presented for the knuckle-leading pantograph for each of the operational heights. Here, the component with the largest drag force is the outer head, which has a value of 183.4 N. Alternatively, the vanes exhibit the lowest drag force, with a value of 8.4 N.

The data indicate a clear trend of increased drag force for increasing height for each of the pantograph components, except for the base, as this is fixed in position. It would be expected that, as each component extends away from the boundary layer surface of the train, it is subject to the higher flow velocity of the free stream. The base section of the assembly remains in position, therefore, the only difference in flow it experiences are due to the modification of the surrounding flow caused by the orientation of other components, specifically on the lower assembly as illustrated in Fig. 8a, b, and c.
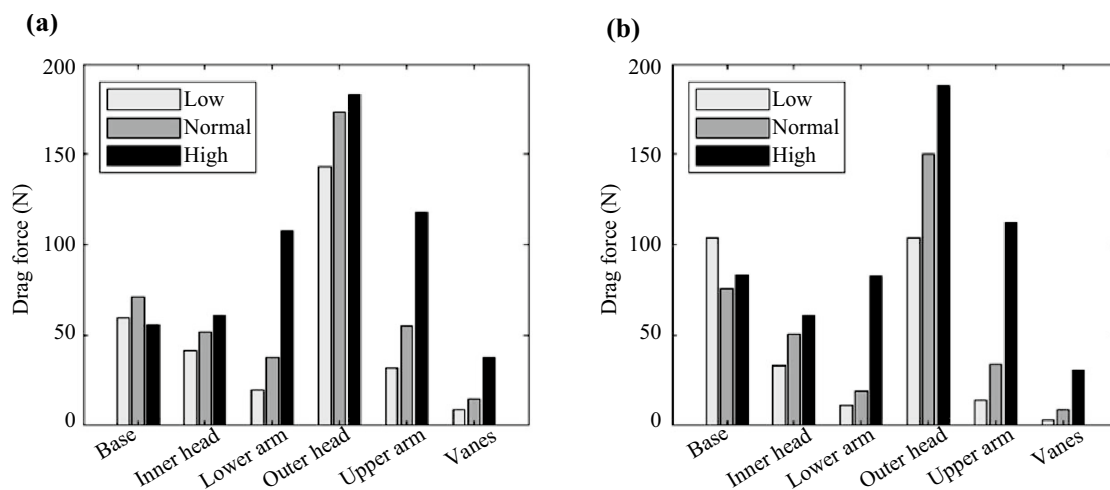
The drag force values for the knuckle-trailing configuration are displayed in Table 4. Here it is clear that the same trend in drag forces is exhibited, with increasing values as the height increases. The maximum drag force is again acting on the outer head, with a value of 188.0 N in the high configuration. Likewise, the lowest drag force is acting on the vanes, with a value of 2.7 N.

Although the largest drag forces are experienced by the outer head section, it is clear that the forces vary significantly on the lower and upper arms with change in pantograph extension. These changes are further illustrated in the bar chart in Fig. 13, for both the knuckle-leading and knuckle-trailing pantograph.

The lift force values for the knuckle-leading pantograph are displayed in Table 5. Here, negative values indicate that the force is acting to push the component downwards. For each of the operational heights, the most significant

Table 4 Drag force values for knuckle-trailing pantograph (unit: N)

Configuration	Base	Lower arm	Vanes	Upper arm	Inner head	Outer head
Low	104.1	11.1	2.7	14.1	33.1	104.0
Normal	75.4	18.9	8.6	33.8	50.2	150.0
High	83.3	82.7	30.8	112.1	60.8	188.0

Fig. 13 Drag force values for **a** knuckle-leading and **b** knuckle-trailing pantograph

Table 5 Lift force values for knuckle-leading pantograph (unit: N)

Configuration	Base	Lower arm	Vanes	Upper arm	Inner head	Outer head
Low	− 16.2	− 15.0	− 27.4	− 9.5	6.1	− 25.5
Normal	− 9.1	− 4.6	− 39.8	− 20.0	8.7	− 34.5
High	− 6.9	38.7	− 104.2	− 63.2	17.4	− 39.7

contributor to the lift force is the vanes, with a value of -27.4, -39.8 and -104.2 N for the low, normal, and high configurations, respectively. The only components that provide a net upward force is the inner head and the lower arm in the heigh configuration. The lower arm transitions from providing a net downward force to an upward force as the height increases.

The lift force values for the pantograph in the knuckle-trailing configuration are displayed in Table 6. The majority of the components are acting with a positive lift force, with the exception of the lower arm and the outer head. As with the knuckle-leading orientation, the vanes are the most significant contributor to the lift force, with a value of 13.9, 34.5, and 91.0 N for the low, normal, and high configurations, respectively. The lift force values of the outer head are comparatively similar for both orientations, whereas the drag force values exhibit larger differences.

To further illustrate the lift force values, Fig. 14 shows bar charts of the component forces in the knuckle-leading and knuckle-trailing orientations.

Neglecting the forces acting on the base, as these do not contribute to forces of the pantograph head on the overhead system, the total aerodynamic drag is compared for each configuration and orientation. For the knuckle leading case, the total aerodynamic drag force is 243.9, 332.1, and 507.6 N for the low, normal, and high configuration, respectively. The

outer head section experiences the largest proportion of the aerodynamic load, accounting for 58.6%, 52.2%, and 36.1% of the total force, respectively. However, as the pantograph height increases, the increased angle of the arms begins to contribute significantly more to the overall force. For the knuckle-trailing configuration, the total aerodynamic drag force is 165.0, 261.6, and 474.4 N for the low, normal, and high configuration, respectively. It is clear from these values that the knuckle-leading pantograph experiences the highest drag forces. This result is in contrast to that described by Li et al. [8], which highlights the importance of considering the train geometry and the pantograph positioning within it. It is clear from the velocity magnitude contours in Fig. 8, that the boundary layer height forming towards the rear of the train is larger than that at the front, resulting in the pantograph experiencing lower relative velocity flow conditions. Again, the outer head sections experience the most significant drag forces, accounting for 63%, 57.3%, and 39.6% for the total forces, respectively.

It should be noted that the lift forces on the pantograph components for the knuckle-leading (Table 5) and knuckle-trailing (Table 6) configurations cannot be summed and seen as the net uplift force that will be applied on the catenary. In the multibody formulation, these forces are applied individually in the pantograph parts, which are connected with different types of joints and suspension elements. This means that

Table 6 Lift force values for knuckle-trailing pantograph (unit: N)

Configuration	Base	Lower arm	Vanes	Upper arm	Inner head	Outer head
Low	8.2	-1.6	13.9	2.5	8.0	-24.3
Normal	8.4	-16.1	34.5	4.5	14.4	-30.1
High	2.6	-75.4	91.0	65.2	15.8	-36.7
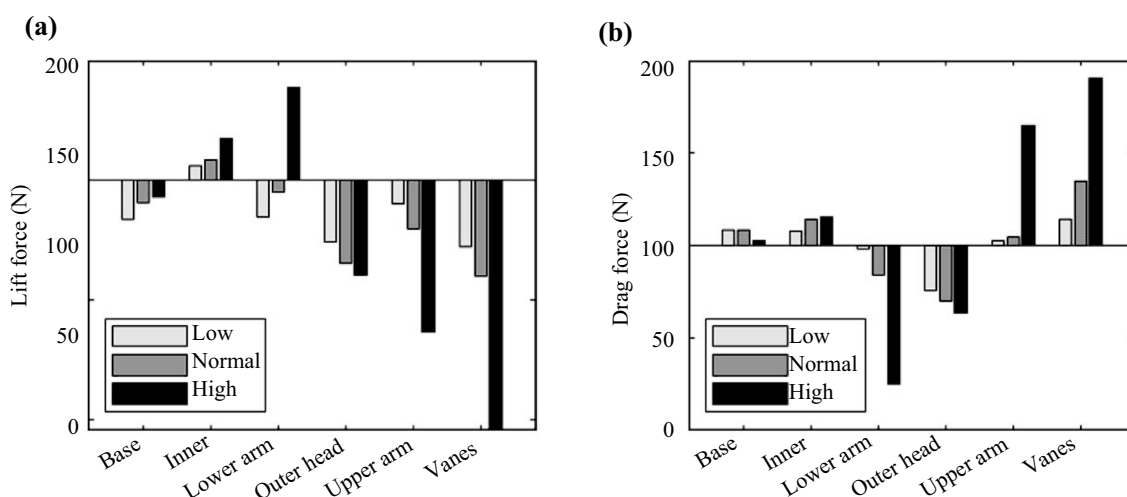
Fig. 14 Lift force values for **a** knuckle-leading and **b** knuckle-trailing pantograph

these forces will be distributed by all elements of the pantograph and not directly applied through the pantograph head.

4 Application scenario

In this section, the pantograph aerodynamic forces are combined with multibody simulations in order to understand how the total upward force, which varies with the pantograph orientation and extension, affects the current collection performance.

4.1 Pantograph and catenary modelling

The analysis of pantograph–catenary interaction is performed here with the computational tool Pantocat [22]. It is a computational tool able to analyse, in realistic operation conditions, models of complete overhead energy collecting systems that include all mechanical details of the pantograph components and the complete topology and structural details of the catenary. PantoCat uses the finite element methodology to study the catenary and the multibody formulation to represent the pantograph [23–25]. These methodologies are integrated via an efficient co-simulation procedure [26, 27], where a contact model based on a penalty formulation is used to represent the pantograph–catenary interaction [28]. PantoCat is extensively used in research and consultancy projects for the rail industry, being currently certified by a notified body to the EN50318:2018.

PantoCat is a fully three-dimensional tool, enabling to model rigid and flexible catenaries with multiple sections, including their overlaps and gradients, the operation of multiple pantographs [29, 30] and consider complex loads on the components, including aerodynamic effects [24, 31]. In the application scenario considered here, depicted in Fig. 15, the catenary includes wire gradients of 1:250, i.e. the wire height changes 1 m for every 250 m travelled along the track.
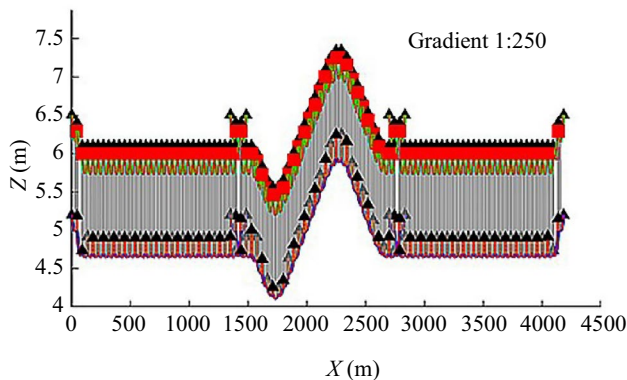
In this case, the contact wire height varies between 4.16 m, representing the train passing under a bridge, and 5.94 m, replicating the railway vehicle passing in a level crossing. In this analysis, only the knuckle-leading pantograph configuration is considered, as the procedure would remain the same for the knuckle-trailing arrangement.

The aerodynamic loads obtained for the low, normal and high configurations are interpolated, creating a force profile according to the vertical position of each pantograph component. This way, as the pantograph travels along the catenary with gradients, its operating height changes and, consequently, the aerodynamic loads vary accordingly, which will affect the dynamic performance of the current collection system. The vertical force for each pantograph component is depicted in Fig. 16.

4.2 Pantograph without aerodynamics loads

The contact force history of a multibody pantograph, without aerodynamic loads, travelling along the catenary model, is presented in Fig. 17. Here, the leading pantograph is considered for the comparative analysis. The area shaded in grey corresponds to an overlap zone between two wire runs of the catenary model.

The only force acting on the pantograph is the static force of the actuator, which is constant. Therefore, even though the wire gradients force the pantograph down and up, the contact force profile developed remains similar across the entire area of interest studied.

4.3 Pantograph with aerodynamics loads

The contact force history of a multibody pantograph with aerodynamic loads included is presented in Fig. 18. The results exhibit significant variations when compared to the
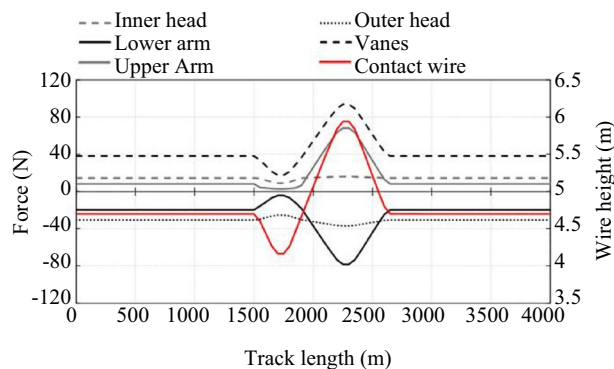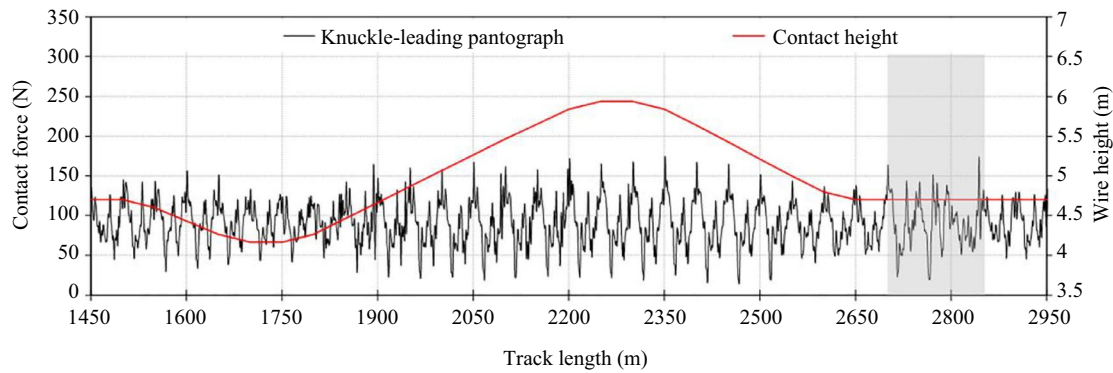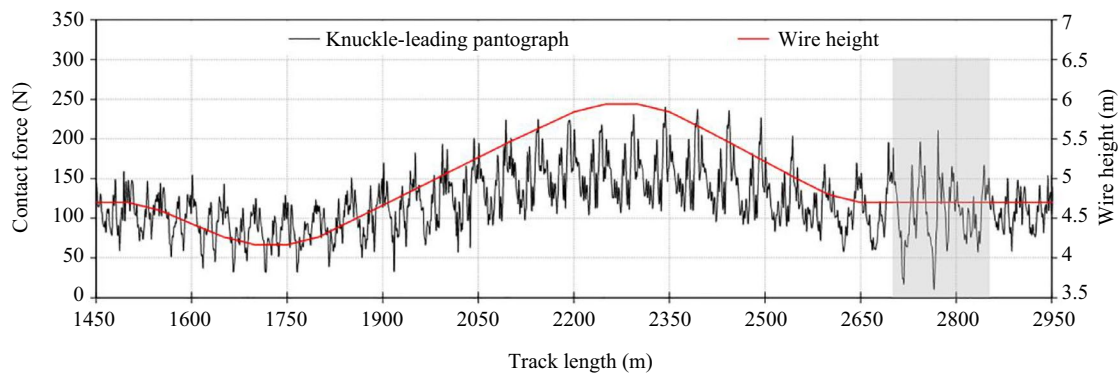

Fig. 15 Finite element model of catenary with wire gradients, side view

Fig. 16 Uplift forces and contact wire height as function of the track length

Fig. 17 Contact force history of a multibody pantograph without aerodynamic loads

Fig. 18 Contact force history of a multibody pantograph with aerodynamic loads

previous scenario without external loads. It is observed that the drag and uplift forces that are applied on the pantograph components, as a function of its operating height, result in contact forces that increase in line with the wire height and decrease when passing in the overbridges (at 1750 m). These results are in line with the behaviour that is observed in service.

5 Conclusions

Controlling the uplift force exerted by the pantograph on the overhead contact line is essential as this determines the wear rate and current collection quality. In this paper, the aerodynamic characteristics of the HSX pantograph are explored for different operating heights in both the knuckle-leading and knuckle-trailing orientation. The inclusion of the full class 800 train geometry in the aerodynamic analysis of the pantograph allows for an accurate representation of the flow field, and thus determination of the forces acting on different components of the pantograph. Six components of the pantograph assembly

are chosen for the analysis, and the lift and drag forces acting on each are extracted.

Considering only the aerodynamics perspective, it is found that the knuckle-leading orientation experiences higher drag forces for each operational height of the pantograph. The lift characteristics of each component display a strong dependency on the orientation, due to the asymmetry in the topology. For the knuckle-leading configuration, the overall upward force (neglecting the base) is found to be -71.2, -90.3 and -151.0 N for the low, normal, and high configuration, respectively. Alternatively, for the knuckle-trailing orientation, to lift force is found to be -1.4, 7.3, and 60.0 N, respectively. This, in addition to the drag forces, results in significantly different loads acting on the pantograph assembly. The individual component lift and drag values are included in a multibody formulation in order to determine the net upward force in each configuration. The performance of the multibody model with and without aerodynamic forces is assessed via dynamic analysis, as the pantograph travels along a catenary with contact wire gradients.

The contact force results show that, without considering aerodynamic loads, the performance is similar regardless of the geometry of the catenary and the pantograph extension. Conversely, considering aerodynamic forces allows for a pantograph model that develops higher contact forces the higher the contact wire, and vice versa, which is in line with what is observed in service, giving assurance on the qualitative validation of the methodologies proposed here. It should also be emphasized that this is a general methodology that can be used to study catenary gradients in any scenario, which does not need to be customized to adapt/correlate with specific case studies and can be replicated elsewhere.

References

1. CENLEC (2012) EN-50367:2012 Railway applications—fixed installations and rolling stock in criteria to achieve technical compatibility between pantographs and overhead contact line
2. Pombo J, Ambrósio J, Pereira M et al (2009) Influence of the aerodynamic forces on the pantograph–catenary system for high-speed trains. Veh Syst Dyn 47(11):1327–1347
3. Baker C, Johnson T, Flynn D et al (2019) Train aerodynamics: fundamentals and applications. Elsevier, New York
4. Luo J, Yang Z, Yu C et al (2009) Numerical research on aerodynamic characteristic optimization of pantograph fixing place on high speed train. In: 2nd International Conference on Power Electronics and Intelligent Transportation System (PEITS), Shenzhen, pp 94–97
5. Dai Z, Tian L, Zhou L et al (2022) Numerical simulation and optimization of aerodynamic uplift force of a high-speed pantograph. Railw Eng Sci 30(1):117–128
6. Dai Z, Tian L, Jian D et al (2022) Effect of the strip spacing on the aerodynamic performance of a high-speed double-strip pantograph. Veh Syst Dyn 60(10):3358–3374
7. Xiao C, Yang M, Tan C et al (2020) Effects of platform sinking height on the unsteady aerodynamic performance of high-speed train pantograph. J Wind Eng Ind Aerodyn 204:104284
8. Qing D, Li T, Zhang J et al (2020) Effects of train pantograph operating height on aerodynamic performance. Sci Sin Technol 50(3):335–345 (in Chinese)
9. Li X, Zhou D, Jia L et al (2018) Effects of yaw angle on the unsteady aerodynamic performance of the pantograph of a high-speed train under crosswind. J Wind Eng Ind Aerodyn 182:49–60
10. Mohebbi M, Rezvani MA (2018) Multi objective optimization of aerodynamic design of high speed railway windbreaks using Lattice Boltzmann method and wind tunnel test results. Int J Rail Transport 6(3):183–201
11. Mohebbi M, Safaee AM (2022) The optimum model determination of porous barriers in high-speed tracks. Proc Inst Mech Eng Part F J Rail Rapid Transit 236(1):15–25
12. Mohebbi M, Rezvani MA (2019) Analysis of the effects of lateral wind on a high speed train on a double routed railway track with porous shelters. J Wind Eng Ind Aerodyn 184:116–127
13. Kim H, Hu Z, Thompson D (2020) Effect of cavity flow control on high-speed train pantograph and roof aerodynamic noise. Railw Eng Sci 28(1):54–74
14. Zhang Y, Zhang J, Li T et al (2017) Investigation of the aeroacoustic behavior and aerodynamic noise of a high-speed train pantograph. Sci China Technol Sci 60(4):561–575
15. AbdelGawad AF, Aljameel NM, Shaltout RE (2022) Computational modelling of the aerodynamic noise of the full-scale pantograph of high-speed trains. J Adv Res Fluid Mech Therm Sci 93(1):94–109
16. Ji Z, Guo Y, Guo D et al (2021) Effects of running speed on coupling between pantograph of high-speed train and tunnel based on aerodynamics and multi-body dynamics coupling. Appl Sci 11(21):10008
17. Niu J, Zhou D, Liang X et al (2018) Numerical simulation of the Reynolds number effect on the aerodynamic pressure in tunnels. J Wind Eng Ind Aerodyn 173:187–198
18. Li R, Zhang W, Ning Z et al (2017) Influence of a high-speed train passing through a tunnel on pantograph aerodynamics and pantograph–catenary interaction. Proc Inst Mech Eng Part F J Rail Rapid Transit 231(2):198–210
19. Carnevale M, Facchinetti A, Rocchi D (2017) Procedure to assess the role of railway pantograph components in generating the aerodynamic uplift. J Wind Eng Ind Aerodyn 160:16–29
20. Carnevale M, Facchinetti A, Maggiori L et al (2016) Computational fluid dynamics as a means of assessing the influence of aerodynamic forces on the mean contact force acting on a pantograph. Proc Inst Mech Eng Part F J Rail Rapid Transit 230(7):1698–1713
21. Menter F (1993) Zonal two equation k-ω turbulence models for aerodynamic flows. In: 23rd Fluid Dynamics, Plasmadynamics, and Lasers Conference, Orlando, AIAA-93-2906
22. Ambrósio J, Pombo J, Antunes P (2015) PantoCat statement of method. Veh Syst Dyn 53(3):314–328
23. Ambrósio J, Rauter F, Pombo J et al (2011) A flexible multibody pantograph model for the analysis of the catenary–pantograph contact. In: Arczewski K, Blajer W, Fraczek J et al (eds) Multibody dynamics: computational methods and applications, vol 23. Springer, Dordrecht
24. Pombo J, Ambrósio J (2012) Influence of pantograph suspension characteristics on the contact quality with the catenary for high speed trains. Comput Struct 110–111:32–42
25. Ambrósio J, Pombo J, Pereira M (2013) Optimization of high-speed railway pantographs for improving pantograph–catenary contact. Theor Appl Mech Lett 3(1):013006
26. Ambrósio J, Pombo J, Rauter F et al (2009) A memory based communication in the co-simulation of multibody and finite element codes for pantograph–catenary interaction simulation. In: Bottasso CL (ed) Multibody dynamics: computational methods and applications, vol 12. Springer, Dordrecht
27. Antunes P, Magalhães H, Ambrósio J et al (2019) A co-simulation approach to the wheel–rail contact with flexible railway track. Multibody Sys Dyn 45(2):245–272

28. Rauter FG, Pombo J, Ambrósio J et al (2007) Contact model for the pantograph–catenary interaction. J Syst Design Dyn 1(3):447–457

29. Pombo J, Ambrósio J (2012) Multiple pantograph interaction with catenaries in high-speed trains. J Comput Nonlinear Dyn 7(4):041008

30. Pombo J, Antunes P (2013) A comparative study between two pantographs in multiple pantograph high-speed operations. Int J Railw Technol 2(1):83–108

31. Pombo J, Ambrósio J (2013) Environmental and track perturbations on multiple pantograph interaction with catenaries in high-speed trains. Comput Struct 124:88–101